Journal of Physics D: Applied Physics

Check for updates

PAPER

OPEN ACCESS

RECEIVED
18 July 2025

REVISED
2 December 2025

ACCEPTED FOR PUBLICATION
10 December 2025

PUBLISHED
24 December 2025

Original Content from this work may be used under the terms of the Creative Commons Attribution 4.0 licence.

Any further distribution of this work must maintain attribution to the author(s) and the title of the work, journal citation and DOI.

Low-power atmospheric-pressure surface-wave microwave discharge in contact with batch and flowing liquids

Kinga Kutasi[1,*], **Cédric Nöel**[2], **Thierry Belmonte**[2] **and Péter Hartmann**[1]

[1] HUN-REN Wigner Research Centre for Physics, Konkoly Thege M. út 29-33, H-1121 Budapest, Hungary
[2] Université de Lorraine, Institut Jean Lamour (IJL), UMR CNRS 7198, Campus ARTEM, allée Andrée Guinier, BP 50840, F-54000 Nancy, France
[*] Author to whom any correspondence should be addressed.

E-mail: kutasi.kinga@wigner.hun-ren.hu

Keywords: surface-wave microwave discharge, plasma–liquid interaction, surfatron launched discharge

Abstract

The operation mode and the characteristics of fully and partially confined surface-wave microwave discharges (SWDs) are determined in the case of freely propagating plasma column and in contact with liquid, respectively. It is shown that the contraction and filamentation of the low-power SWD depend on the input power and gas flow conditions, and are related to the power absorption and radial temperature gradients. The power dependent length of the plasma column shortens with filamentation. The partially confined SWD retains the operation properties of fully confined discharge under the same conditions inside the discharge tube, while outside the tube the discharge contraction and its length are controlled by the air inflow into the plasma plume. As a result of air inflow the electron density increases, and it is further enhanced when brought in contact with water. The water surface hinders the propagation of the surface-wave, thus in the shortened plasma column the power absorption per unit length increases. The contraction of plasma plume ceases when brought in contact with liquid surface, and the filaments cover a surface area comparable to that of the discharge tube. The afterglow flow follows the liquid meniscus and it is deflected accordingly at the edge of the container, while influences the vapour admixture into the plasma and enhances the interfacial processes along the liquid surface.

1. Introduction

The interaction of the atmospheric-pressure discharge plasmas with liquids has been intensively investigated in the case of several type of discharges as reviewed in [1, 2]. The studies have been predominantly motivated by the biological applications of plasma-treated liquids [3–7] and by the purification of water [8–10]. From the applications point of view, in the case of the plasma–liquid interaction, the main interest lies in the deposition of charged and reactive gas phase species created in the plasma into the liquid. Plasma species can be deposited into the liquid either through its interaction with the active or the afterglow plasma [1]. The active plasma can be also electrically coupled with the liquid, when one of the electrodes is the liquid itself [2], or the liquid is part of the electrical circuit [11, 12]. In this case the electrical properties of the liquid, which can change during the plasma operation, can influence the plasma properties [13], as well as the direction of the plasma induced convection in the liquid [14]. In the case of no electrical coupling, the main influence of the liquid on the plasma operation originates from the humidity resulting from the plasma induced evaporation [15].

The present work focuses on a less investigated electrodeless surface-wave microwave discharge (SWD) launched with a surfatron in a quartz tube, and sustained by a surface-wave traveling along the boundary of the plasma column and the dielectric tube. It has been recently demonstrated that the discharge can be applied for efficient deposition of reactive species into liquids [16], which motivates the detailed investigation of the system.

© 2025 The Author(s). Published by IOP Publishing Ltd

The surfatron launched SWDs have been investigated thoroughly in the low-pressure low-power range focusing on both the discharge operation [17, 18] and the chemical kinetics in different gas mixtures [19, 20]. At atmospheric pressure more attention has been given to the high-power molecular discharges [21, 22], and noble gas discharges for analytical plasmas [23].The attention has turned to low-power atmospheric surface-wave discharges with the emergence of plasma medicine and plasma agriculture, where plasma is brought in contact with heat sensitive biological samples or liquids.

Targeting biomedical applications the operation of a low-power surfatron launched SWD has been studied by Krčma *et al* [24]. The appearance and the emission spectra of the discharge has been recorded in the case of different $Ar/N_2/O_2$ gas mixtures using 3 slm flow rate and 25 W input power. The discharge has been sustained in a 2.5 mm inner diameter (ID) tube using a low-power solid-state microwave power supply. In the case of the Ar discharge confined into a 2 mm long tube, the plasma column could extend into the ambient air for a length of 17 mm—which significantly decreased with the addition of few sscm N_2 and O_2, respectively—and featured one single filament. Ridenti *et al* [25] have extended the investigations to input powers up to 150 W for both confined and unconfined discharges. The confined discharge denotes the discharge where the plasma column is confined into the discharge tube at its full length, while in the case of the unconfined discharge the discharge tube does not exit the surfatron body and the plasma column expands at its full length in the free space (usually in the ambient air). The confined discharge has been sustained in a quartz tube of ID 3 mm and OD 5 mm, conditions very similar to those in [24]. The unconfined discharge is ignited in an alumina ceramic tube of ID 2 mm and OD 4 mm. In the confined case at flow rates higher than 2.5 slm and powers above 50 W the single filament doubled into two contracted filaments, while periodic transitions between the modes occurred. The unconfined discharge behaved similarly at higher powers, while below 40 W featured one contracted filament.

The contraction and filamentation of surface-wave discharges have been investigated previously in larger diameter tubes, ID $\geqslant$6 mm, at high input powers, i.e. $P > 100$ W. Castaños *et al* [26] have suggested that the radial contraction occurs due to the non-uniform gas heating through its influence on the molecular ion density, since these ions control the creation and loss of charged particles through stepwise ionisation and dissociative recombination, respectively. Thus, contraction can be related to both the presence of molecular ions and to the non-uniform gas heating [27]. On the other hand, the filamentation, which occurs when the single axially centred filament turns into two or more off-centred filaments, is attributed to the radial non-uniformity of the microwave field intensity, that increases with increasing field frequency and tube radius [27, 28]. Hnilica *et al* [29] have shown that in high power discharges the structure and the dynamics of the filaments depend on the input power and the gas flow rate. The structure and dynamics of the filaments can be important in surface and gas treatment processes, where the spatial and temporal distribution of plasma species in the interaction zone is crucial. In the case of plasma–liquid interaction the density distribution of species on the liquid surface is less crucial, however the temperature distribution—such as the focused hot spots of filaments—can determine the evaporation and species deposition into the liquid.

As presented above, in the low-power range the SWDs ignited in tubes of ID ranging between 1 to 3 mm using gas flow rates of 2.5–5 slm have been investigated. These discharges are characterised by a contracted filament, which divides into two transient filaments with increasing power. One of the aims of the present work is to investigate the operation mode of the SWDs ignited in higher diameter tubes, and the possibily to achieve wider stable plasma columns, while using lower gas flow rates. The dynamics and structure of the filaments, as well as the macroscopic behaviour of the plasma column will be studied. We aim to determine the cause of the filamentation and its effect on the length of the plasma column.

When targeting applications relying on the plasma–liquid interaction, the relevant SWDs are the unconfined or partially confined discharges. In both cases the plasma column extends beyond the discharge tube, as described above. We aim to follow the transition from the fully confined to the partially confined and unconfined discharges, and to determine the effect of different discharge parameters, such as the tube length, gas flow rate and cooling air flow on the characteristics of the plasma column. In general, the plasma parameters can help to understand this transition, and also give support for the design and tuning of the plasma–liquid interaction. Therefore, we aim to map the axial electron density distribution during the transition to the partially confined discharge, as well as when that is brought in contact with the liquid. And finally, the effect of the liquid surface on the plasma propagation and on the afterglow gas flow will be elucidated.

Overall, we aim to address all the discharge characteristics that need to be taken into account in the design of the plasma–liquid interaction system.

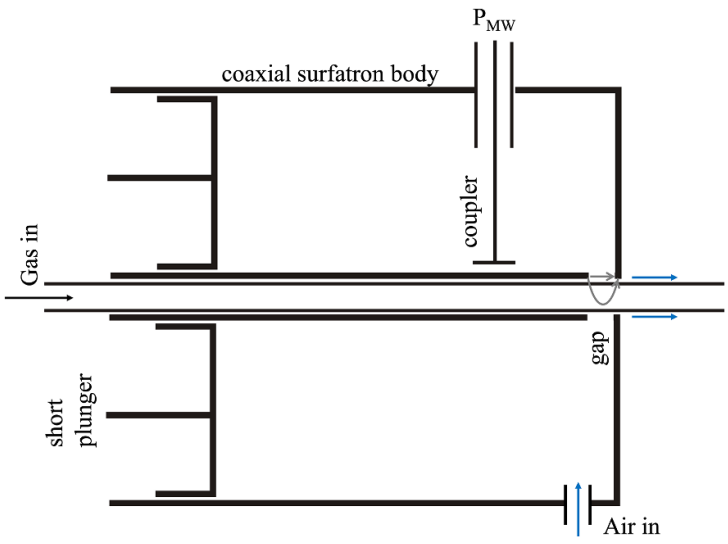


Figure 1. The structure of the surfatron.

2. Experimental methods

2.1. Discharge set-up and imaging methods

The SWD is ignited with the help of a surfatron wave launcher (Sairem, Surfatron 80) powered by CoberMuegge microwave generator (2450 MHz ±10 MHz, 300 W) based on magnetron (TO300-M23 Panasonic). The surfatron is a coaxial waveguide terminated by a short-circuit plunger at one end, and by a launching gap at the other end, as shown in figure 1. The discharge is generated in a quartz tube coaxially positioned into the surfatron body. The microwave field is coupled into the surfatron with a capacitive coupler. The electric field coupled into the coaxial body, which is normal to the coaxial surfaces is changed by the circular gap into an azimuthally symmetric field distribution similar to that of an $m = 0$ mode wave [17, 30]. As a consequence, with the gas breakdown a surface-wave can be launched, which travels on the boundary of the quartz dielectric and the plasma it sustains. The development of the steady-state discharge is presented in section 3.1. The surfatron is designed not only to launch the surface-wave, but also makes possible the impedance matching between the generator and the discharge, namely by tuning the capacitive coupler, the resonator and the gap size [17].

Discharges in different diameter quartz tubes are generated in flowing gas using flow rates in the 0.5–3 slm range stabilised with an Aalborg mass flow controller. The main gas used is Ar of 5.0 purity supplied through stainless steel tubing. The input power is varied in the 15–40 W range. In the present study the surfatron system is positioned vertically.

The operation mode of the discharge is studied through imaging. Image series of the discharge are recorded with the Allied Vision Prosilica GX1050 camera (with quantum efficiency above 350 nm) using the camera control software at 112 fps and exposure times in the 10 μs–20 ms range. In order to reduce the discharge emission intensity during imaging, different bandpass filters have been applied, as shown in figure 2.

The gas flow and the heat transport in the discharge region and at plasma–liquid interface is visualised with the help of a single-mirror coincident Schlieren system. In general, the Schlieren imaging detects the change of the refractive index of a transparent medium in the test area, which can be caused by changes in the density, temperature, or pressure. In the case of the single mirror set-up the test area is located in front of a spherical mirror. The present system consists of an LED flashlight equipped with a pinhole in order to create a point light source, and a spherical mirror of 10 cm diameter and 50 cm focal length. The light source—illuminating the discharge tube—is positioned off-axis in the double focus of the mirror. The mirror creates the image of the light source symmetrically in the double focus, where a knife-edge is placed to block the light of the source entering the camera. Meanwhile, in the test area the light is deflected due to the change of the refractivity. The camera, an Allied Vision Prosilica GX1050 camera (112 fps), placed behind the knife-edge and focused on the discharge tube collects only this deflected light, which gives rise to the Schlieren image.

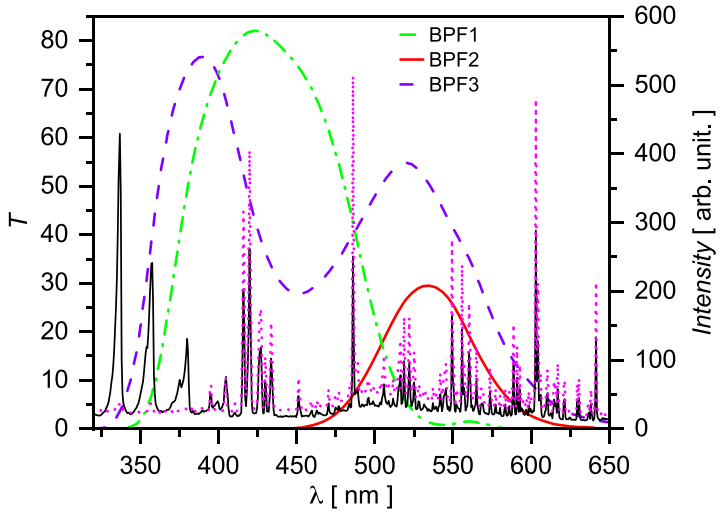


Figure 2. The transmission of the optical bandpass filters used during imaging, and characteristic spectra of the discharge inside (dashed line) and outside (full line) of the discharge tube, respectively, measured with Avantes spectrometer (AvaSpec-ULS2048x64TEC-EVO) with a 20 μm entrance slit.

2.2. Determination of the electron density

The electron density is determined from the Stark broadening of the Hα line, which results from the perturbation of the upper level of H atoms originating from the long range interactions with the charged particles. According to the calculations of Gigosos M A and Cardeñoso [31] the Stark broadening depends on the electron density as follows : $n_e(\mathrm{cm}^{-3}) = 8.8308 \times 10^{16}(\Delta\lambda_S(\mathrm{nm}))^{1.6005}$ [32]. In order to calculate the electron density the Stark broadening is determined from the experimental line profile as follows.

Generally, in the case of atmospheric pressure discharges, the profiles of the atomic spectral lines can be approximated by a Voigt function, resulting from the convolution of a Gaussian function and a Lorentz function. The Gaussian part of the profile corresponds to the contributions of the instrumental broadening and the Doppler broadening, while the Lorentzian profile results from the van der Waals broadening and Stark broadening. The width (full width at half-maximum) of the Gaussian $\Delta\lambda_G$ and of the Lorentzian ($\Delta\lambda_L$) profiles can be obtained from the deconvolution of the recorded experimental profile.

The width of the Gaussian profile composed of the instrumental ($\Delta\lambda_{inst}$) and the Doppler ($\Delta\lambda_D$) broadenings can be expressed as $\Delta\lambda_G = \sqrt{\Delta\lambda_{inst}^2 + \Delta\lambda_D^2}$. The Doppler broadening is caused by the isotropic thermal motion of H atoms, and is given by $\Delta\lambda_D(\mathrm{nm}) = 4.703\times10^{-4}\sqrt{T_{gas}(\mathrm{K})}$.

The width of the Lorentzian profile resulting from the van der Waals broadening ($\Delta\lambda_{vdW}$) and Stark broadening ($\Delta\lambda_S$) is given by the $\Delta\lambda_L = \Delta\lambda_{vdW} + \Delta\lambda_S$ expression. The van der Waals broadening occurs from the perturbation of the upper level ($n = 3$) of H atoms due to the van der Waals interaction with neutral species, and thus it depends on the total neutral density (i.e. pressure and gas temperature). It has been previously shown, that under similar conditions at atmospheric pressure the van der Waals broadening of the Hα line can be estimated as $\Delta\lambda_{vdW}$ (nm) $= 5.736/T_{gas}(\mathrm{K})$ [33]. With the knowledge of the gas temperature, and consequently of the van der Waals broadening, the Stark broadening can be calculated as $\Delta\lambda_S = \Delta\lambda_L - \Delta\lambda_{vdW}$.

During the fitting procedure of the Voigt profile, the Gaussian broadening is treated as a fixed parameter. Its value is established for each experimental condition according to the formula given above, as follows: the instrumental broadening is set to the measured constant value of 0.03 nm, while the Doppler broadening is calculated based on the measured gas temperature. The Lorentzian broadening is a free parameter. From the value obtained after fitting, and after subtracting the van der Waals broadening (calculated from the gas temperature), the Stark broadening is obtained, allowing the electron density to be determined. This fitting procedure results in a typical uncertainty between 2 to 5 $\times10^{13}$ cm^{-3} in the electron density values.

The gas temperature is considered to be equal to the rotational temperature of OH molecules resulting from the dissociation of the water molecules present in the system as impurities [34, 35]. The temperature is determined from the rotational spectrum of the OH ($A^2\Sigma^+$—$X^2\Pi$) system. Assuming a partial local thermodynamic equilibrium and a Boltzmann distribution function for the rotational

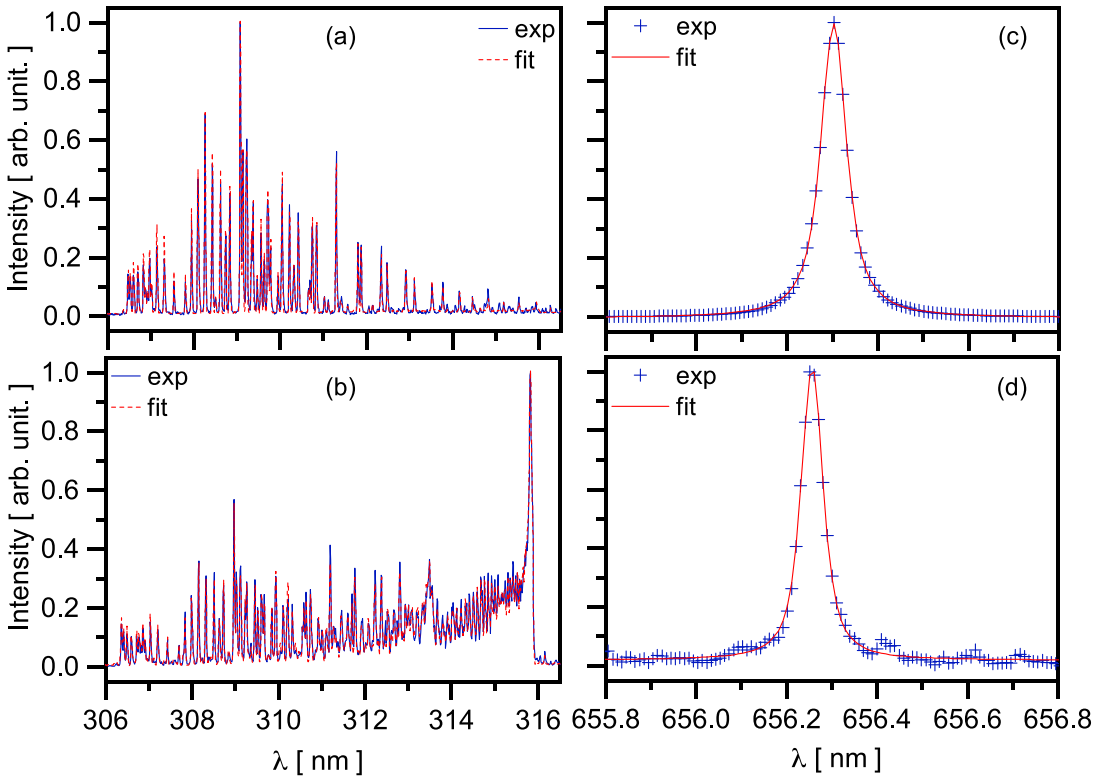


Figure 3. The high resolution emission spectra of OH ($A^2\Sigma^+$—$X^2\Pi$) system and Hα line measured in the confined discharge (a) and (c) and in the plasma plume (b) and (d), respectively.

levels, a simulated spectrum is calculated for a given temperature ($T_{rot} \approx T_{gas}$) [36, 37]. During spectra simulation the N_2 and NH emissions in the same spectra range are also taken into account. The T_{gas} is determined by fitting the simulated spectrum to the recorded emission spectrum using a self-developed Python code based on least squares method. The measured and fitted spectra are illustrated for two cases in figures 3(a) and (b).

The high resolution spectra of the OH ($A^2\Sigma^+$—$X^2\Pi$) emission in the 303–320 nm spectral range, and of Hα line in the 655.5–657 nm range have been recorded with a Carl Zeiss Jena PGS-2 spectrograph equipped with a greateyes ELSEs 2k512 BI UV3 detector. The emission light is collected through a 10 mm wide collimator equipped with a 1 mm slit, and guided through the optical fiber to the 20 μm wide entrance slit of the spectrograph. The instrumental broadening $\Delta\lambda_{inst}$ is measured to be 0.03 nm.

3. Results and discussion

3.1. Operation modes

3.1.1. Fully confined discharges

The discharge is sustained by the surface-wave launched at the surfatron gap with the gas breakdown and propagating along the boundary of the plasma column and the quartz dielectric. The development of the plasma column is insured by the ponderomotive force acting on the electrons due to the large axial field gradient developed in the gap region with the gas breakdown—or at the end of the not fully developed plasma column—which drives the electrons along the axis [38]. The electrons gain energy from the electromagnetic field and lose most of their energy in inelastic collisions, which insures the build up of the plasma density. Once the electron density exceeds the critical electron density[3] in the breakdown area, the surface-wave propagates till the point where the electron density falls below the critical electron density. At this wave reflection point a large axial field gradient develops, which results in

[3] The critical electron density is determined from the propagation condition of the surface-wave. The surface-wave propagating along the boundary of the plasma column and the quartz dielectric (ϵ_d) has the wavenumber of $k_z = \frac{\omega_{pe}}{\omega}\sqrt{\epsilon_d \frac{\omega_{pe}^2-\omega^2}{\omega_{pe}^2-(1+\epsilon_d)\omega^2}}$. Consequently, the surface wave can propagate if $\omega_{pe}^2 > (1+\epsilon_d)\omega^2$, where ω and ω_{pe} are the field and the plasma frequencies, respectively. This condition determines the critical electron density that is $n_{ec} = (1+\epsilon_d)\omega^2 m_e \epsilon_0 / e^2$.

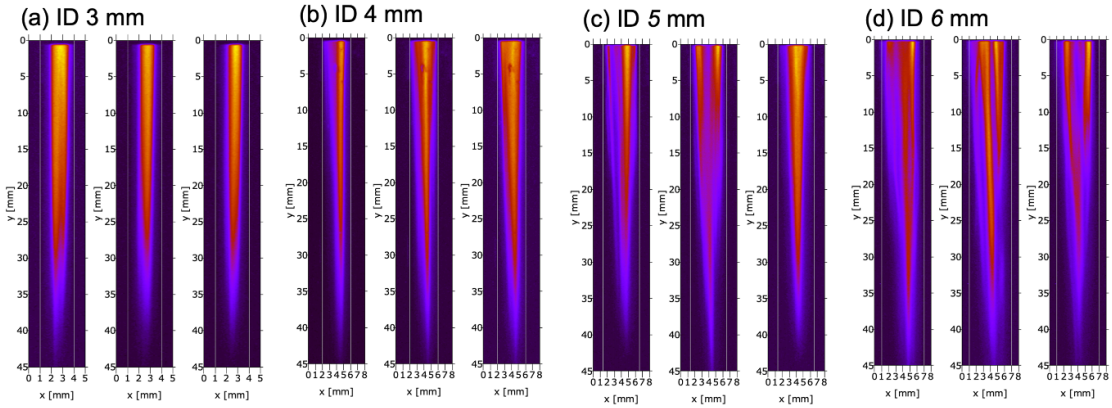


Figure 4. Sequence of false-colour CCD images of discharges ignited in different inner diameter (ID) tubes and sustained at 24 W power under 2 slm Ar flow rate. Images are recorded with 20 ms exposure time and 55 fps (i.e. ≈9 ms apart) during the continuous operation of the discharge with the application of the BF2 (450–650 nm) bandpass filter.

the forward ejection of the electrons and in this way, the development of a new plasma column segment. This process continues until the plasma column fully develops, which depends on the gas characteristics and the input power.

The fundamental TEM mode of the microwave field is coupled into the surfatron with a capacitor plate positioned parallel to the inner tube of the coaxial structure, and the surface-wave is launched at the cylindrically symmetric gap. Due to this symmetry the only surface-wave mode appreciably excited shall be the azimuthally symmetric mode with $m = 0$, where m is the wavenumber corresponding to the azimuthal angle, which is a purely TM mode[4] [39, 40]. Nevertheless, azimuthal inhomogeneity introduced in the field at the gap by the feeding coupler may occur, and thus the field intensity at the gap can be the summation of field components of different azimuthal configurations [40]. As a consequence, provided the discharge stability criterion is satisfied, the $m = 1$ mode surface-wave may be also excited. According to the calculations of Margot-Chaker *et al* [40] this criterion is $\omega R \geqslant 2\,\mathrm{GHz\,cm^{-1}}$, where ω is the field frequency and R the inner tube radius. In the present work, discharges ignited in tubes of ID ranging between 3–6 mm are studied, which do not satisfy the criteria of the $m = 1$ mode excitation.

Figure 4 illustrates the macroscopic behaviour of the discharges ignited in 65 mm long tubes through sequences of false-colour CCD images recorded with 55 fps at 24 W under 2 slm Ar flow, where stable and fully developed plasma columns are obtained in the case of all investigated discharge tubes. The images show that in the case of the two lower diameter tubes, i.e. ID 3 mm and 4 mm, the discharges are characterised by one central filament, which may indicate the $m = 0$ operation mode. On the other hand, in the case of the ID 5 mm and 6 mm tubes the discharges are characterised by both static and dynamic filaments. The two static filaments would suggest an $m = 1$ operation mode, while the dynamic filaments can give to the discharge a transient behaviour and make it to oscillate between the two operation modes. The radial intensity distributions—deduced from a sequence of images—at the surfatron exit, as shown in figure 5, indicate that the transient behaviour of the discharge occurs in the case of all the investigated tubes and strongly depends on the input power. Same behaviour has been observed by Ridenti *et al* [25] in the case of ID 3 mm tube, stating that at flow rates higher than 2.5 slm and powers above 50 W the single filament doubled into two contracted filaments and periodic transition between the modes occurred.

The transient behaviour of the surfatron generated SWD with power is illustrated in the case of the 4 mm ID tube in figure 6. At the low input power of 18 W, where a stable self-sustained discharge is obtained, the discharge is composed of one dynamic filament which covers the whole cross section of the tube, as shown by the radial images in figure 6(b) . With increasing power, at 22 W (figure 6(a)) the filament tends to localise in the central part of the tube. However, this filament is not fully static, as indicated by the sequence of images shown for 24 W in figure 6(b). In the case of the ID 4 mm tube this quasi-static filament can be achieved in the 20–26 W power range. In the case of the higher diameter

[4] In a cylindrical configuration this mode has a non-zero electric field in the radial, E_r, and axial, E_x, directions, while the magnetic field component in the azimuthal direction, H_Φ.

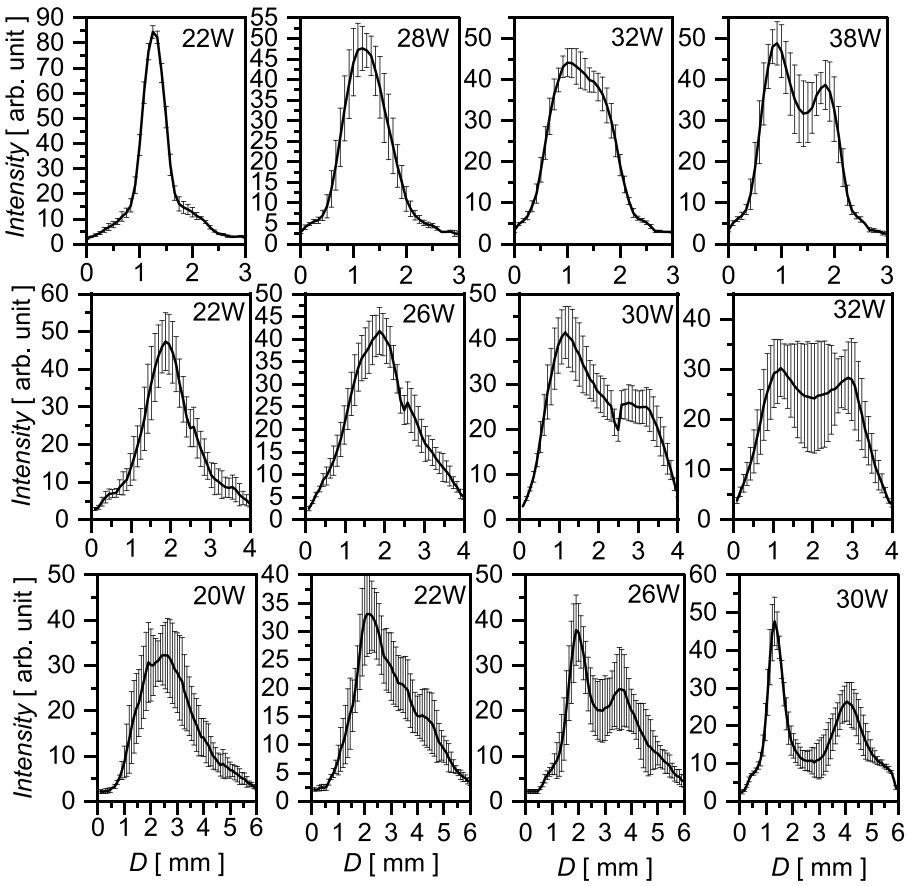


Figure 5. Radial emission intensity distributions deduced from the CCD images for ID 3 mm (1st row), 4 mm (2nd row) and 6 mm (3rd row) tubes at 4 mm distance from the surfatron's end plate.

6 mm tube, as indicated by figure 5 this power range is very narrow, namely between 18–20 W. With further increase of power, besides the quasi-static filament, a second dynamic filament appears (as shown in figure 6(a) for 26 W), which in the case of the ID 6 mm tube becomes quasi-static above 30 W, while in the case of the ID 4 mm tube above 32 W, as shown in figure 6(b).

In the case of high power SWDs (P>150 W) ignited with the help of a surfaguide in an ID 6 mm tube—where only stable filaments are suggested to exist—the contraction and filamentation has been attributed to the non-uniform gas heating and to the radial non-uniformity of the microwave field intensity, respectively [27, 46]. In general, the gas temperature profile may be influenced by the gas flow rate used and the tube diameter. The effect of the gas flow rate is investigated in the case of the ID 6 mm tube at 34 W, where two stable filaments can be obtained under the 2 slm Ar flow condition. Figure 7 shows the false-colour CCD images of discharges ignited in ID 6 mm tube sustained at 34 W power under different Ar gas flow rates. We note, that in order to ensure the symmetry it is crucial the perfect coaxial positioning of the tube into the surfatron body. At the lowest 0.1 slm gas flow rate a contracted—all along the plasma column—single filament discharge is obtained with a dynamic sheath. In the vicinity of the launcher the filament widens and the sheath becomes more diffuse with increasing gas flow rate, while the filament remains contracted downstream the plasma column. With the further increase of the gas flow rate—at around 0.4 slm—the widened filament splits into two filaments, which merge downstream. The radial images in figure 8 taken with 100 μs exposure time indicate that at low gas flow rates the central contracted filament is static, while at high gas flow rates the two off-centred filaments are dynamic, i.e. they are circulating around the axis.

At low gas flow rates one can expect higher gas temperatures. The increase of the gas temperature decreases the gas number density and consequently can lead to the increase of the mean free path of the electrons. The average gas temperature shown in figure 9 is determined at 2 mm distance from the launcher from the rotational spectra of OH molecules. The measurement indicates the decrease of gas temperature with the gas flow rate, namely the gas temperature drops from 1800 K to 1200 K when gas flow rate increases from 0.1 slm to 1.5 slm. At the same time, the emission intensity of the 750.3 nm

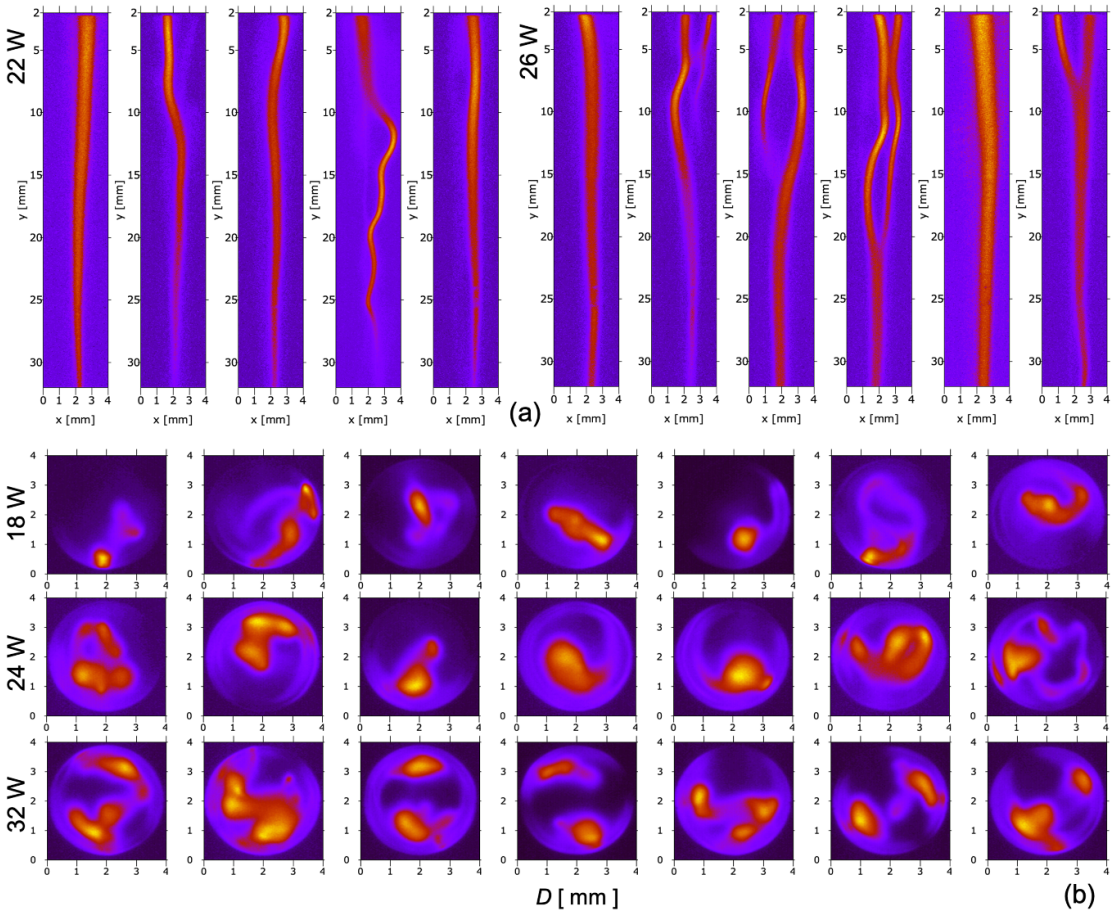


Figure 6. Sequence of false-colour CCD images of the ID 4 mm discharge for different input powers at 2 slm Ar flow rate. Images are recorded with 20 μs exposure time and and 55 fps during the continuous operation of the discharge.

Ar line, which is the result of electron excitation of Ar atoms, increases. The data clearly indicate the increase of the gas number density with the gas flow rate. Furthermore, a temperature gradient—thus a number density gradient—towards the walls also exists, which is partially determined by the convective term of the velocity profile, i.e. the gas flow rate and the tube's ID.

The effect of the gas temperature's radial profile on the plasma contraction along the plasma column has been studied my means of modelling without taking into account the effect of gas flow, by Castaños *et al* [26] in case of high power discharges. The decrease of the gas temperature, i.e. increase of the gas density, towards the walls results in the increase of the collisional frequency, which is concluded to enhance the inhomogeneity of the radial field. Downstream the plasma column, due to the decrease of the absorbed power density, lower temperature gradients are obtained and less inhomogeneous fields, while the plasma becomes more contracted. It is concluded, that the increasing radial inhomogeneity of the electric field intensity reduces the radial contraction of microwave discharges. In principle the size of the sheath is correlated with the temperature gradient.

When taking into account the gas flow, at low flow rates a more homogeneous radial temperature distribution is expected with a sharp decrease close to the walls. In this case the collisional frequency is enhanced in a very narrow region near the walls, while—according to the measured high gas temperature—is reduced across the tube radius. In this case a more contracted plasma and a large sheath is obtained. With increasing gas flow rate, i.e. the gas velocity, the temperature gradient covers a larger section of the tube leading to enhanced radial field inhomogeneity and shorter sheath, as illustrated in figure 10. Due to the enhanced collision frequency, the radial energy deposition of electrons occurs in a shorter distance, resulting in the splitting of the one central filament into two filaments. In the case of the ID 4 mm tube due to the smaller diameter this effect occurs at higher gas flow rate, shown in figure 10(c).

With increasing gas flow rate the length of the plasma column increases, as long as the plasma is characterised by one central filament. Similar effect is achieved with increasing power under constant gas flow rate. In general, the length of the plasma column increases with the input power while it is

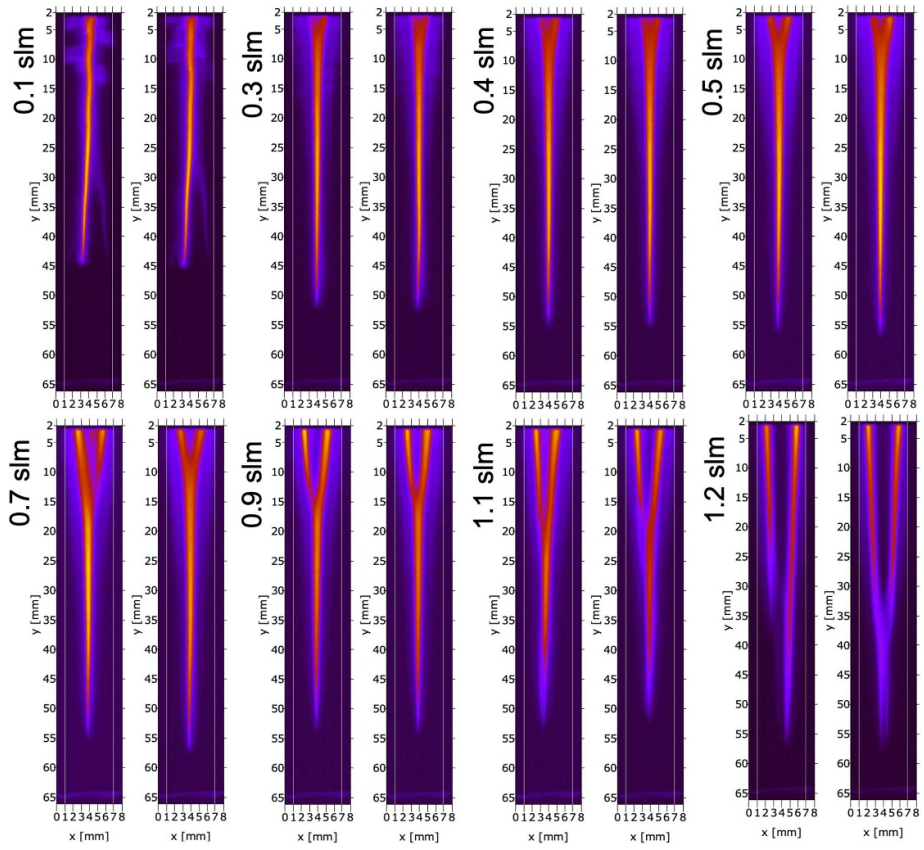


Figure 7. Sequence of false-colour CCD images of the ID 6 mm discharge at 34 W power under different Ar gas flow rates. Images are taken with 10 ms exposure time and 55 fps during the continuous operation of the discharge with the application of the BF1 (350–550 nm) bandpass filter.

composed of one dynamic or one quasi-static filament, and it starts to decrease with the appearance of a second quasi-static filament. Figure 11 shows the average axial distribution of the radially integrated intensity deduced from the sequence of images recorded with 20 ms exposure time for three different ID discharge tubes. The axial intensity distributions indicate that longer plasma columns can be obtained in smaller diameter tubes, where the second dynamic filament appears at higher powers.

According to the calculations of Castaños *et al* [26], the contracted plasma is associated with lower power absorption, which can result in longer plasma column at increasing input power. On the other hand, the non-contracted plasma column, associated with enhanced collisional frequency, is related to higher power absorption[5], that can lead to shorter plasma column.

3.1.2. Partially confined discharges

When targeting plasma-surface interaction, plasma jets or unconfined plasma columns are aimed for. Unconfined plasma column, i.e. plasma plume, can be provided with partially confined discharges achieved by shortening the discharge tube at confined discharge conditions. In the case of the unconfined plasma column two major conditions differ from that of the confined case: (*i*) the boundary the surface-wave propagates on changes from the plasma-dielectric to the plasma-air and (*ii*) the discharge is sustained in the mixture of the input gas and the air diffused into the plasma plume. As a consequence, the length of the plasma column can significantly change compared to the confined case. Additionally, the cooling air applied along the tube, which exits the surfatron body with a high convective velocity in a narrow ≈0.1 mm gap around the tube, strongly influences the air-plasma interaction along the plasma column. Figure 12 shows the radially integrated emission intensity along the plasma column for three

[5] The power absorbed by the electron is $u = \frac{(eE)^2\nu_c}{2m(\nu_c^2+\omega^2)}$, where ν_c and ω are the electron collision and field frequencies, respectively, E is the sustaining field, and e and m are the absolute value of the electron charge and the electron mass, respectively. The power gain is maximum when $\nu_c = \omega$.

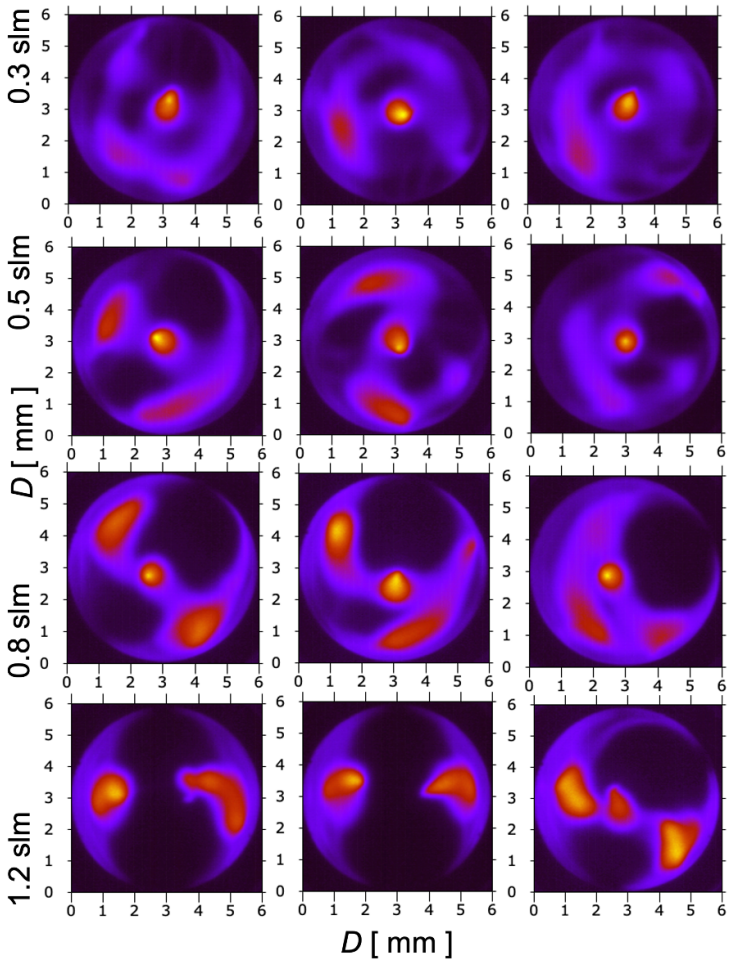


Figure 8. Sequence of false-colour CCD images of the ID 6 mm discharge at 34 W power under different Ar gas flow rates. Images are taken with 100 μs exposure time and 55 fps during the continuous operation of the discharge.

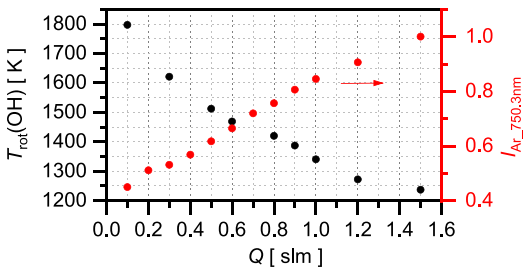


Figure 9. The OH rotational temperature and the 750.3 nm Ar line emission intensity—normalised to the maximum absolute intensity—as a function of Ar gas flow rates measured at 4 mm distance from the surfatron's end plate in the case of the ID 6 mm discharge sustained with 34 W power.

different length of the discharge tube and cooling air flow rates, respectively. The shortening of the discharge tube results in the decrease of the plasma column, while the increase of the air flow rate further quenches the plasma plume. In the case of short discharge tubes, such as 1 mm and 15 mm, plasma plumes of a significant length are obtained. The length of these plasma plumes are similar and the recorded spectra do not show significant differences. The spectra indicate the increase of the air inflow to the plasma plume with the increase of air flow rate, i.e. the emission of nitrogen increases, while that of Ar decreases at a given position of the plasma plume. The used surfatron is designed for OD 8 mm tubes, thus using smaller diameter tubes, i.e. widening the airstream outlet, the convective velocity of air decreases and becomes more diffuse downstream the plasma column. In this way, while providing similar cooling to the tube wall in the vicinity of the surfatron, the quenching effect of the airstream can be reduced/controlled.

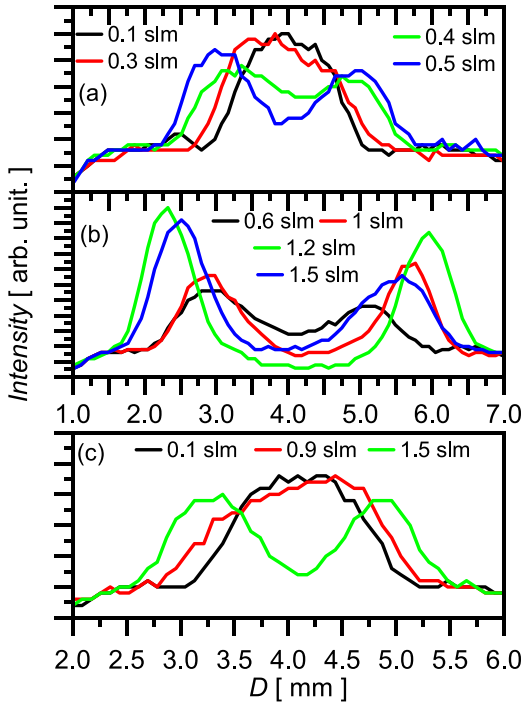


Figure 10. Radial emission intensity distributions at 3 mm axial position deduced from the CCD images for the ID 6 mm (a) and (b) and ID 4 mm (c) discharges sustained with 34 W power at different Ar gas flow rates.

The partially confined discharges retain the properties of the confined discharges inside the discharge tube. Similarly to the confined discharge, the increase of the discharge gas flow rate induces filamentation inside the discharge tube, as shown in figure 13. However, outside the discharge tube the plasma is contracted into one central filament, even at conditions where two stable filaments exist in the confined discharge, such as at gas flow rates higher than 1.2 slm in the ID 6 mm discharge (figure 7). The contraction of the plasma in this region is controlled by two factors: the radial temperature gradient and the increased collisional frequency due to the inflow of molecular gases. The plasma plume becomes more diffuse with the increase of the air flow, i.e. with the increase of air admixture in the plume. In the plasma plume with the increase of the Ar gas flow rate the air inflow can be reduced, which results in the significant increase of the plasma plume's axial extension. A further increase of the length of plasma plume can also be obtained with the increase of the input power, similarly to the confined discharge.

3.2. Characteristics of the plasma column

The characteristics of the plasma column are studied in the case of the discharge configuration chosen for liquid treatments. In the previous section it has been shown that with increasing the tube diameter, from 3 mm to 6 mm, the power range where a single filament operation can be achieved is narrower, and the appearance of the second filament leads to the decrease of the plasma length. On the other hand, the single filament plasma column and the plasma plume become more contracted with decreasing tube diameter. Additionally, under the same gas flow conditions the gas velocity increases with decreasing tube ID, which can lead to cavity formation in the liquid surface. Although the higher gas flow rates favour filamentation, the application of gas flow rates higher than 1 slm is required, since at lower gas flow rates the plasma column is more contracted and the plasma plume is very short, which limits the tuning possibilities of the plasma–liquid interaction. These findings confirm, that the previously used system [16, 41, 42], namely ID 4 mm and 2 slm Ar, chosen exclusively based on the performance in RONS deposition, is a quasi-optimal system that allows tuning of plasma–liquid interaction in a wider range. Furthermore, with the reduction of the tube's outer diameter to 6 mm the quenching effect of the cooling air flow can be controlled, as discussed in the previous paragraph.

In the case of plasma treatment of liquids, as previously shown e.g. in [16, 41, 43], the electrons play an important role in the creation of reactive oxygen and nitrogen species, primarily in that of H_2O_2, at the plasma–liquid interface. Furthermore, the electrons injected into the liquid, which become solvated electrons, can drive electrochemical reactions in the liquid phase [43–45]. In order to show the

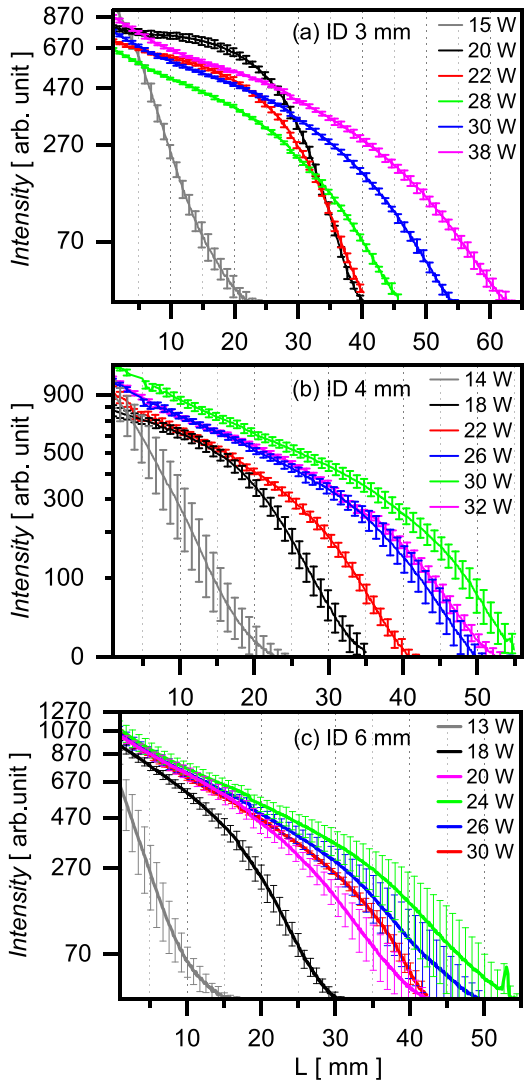


Figure 11. Average axial emission intensity distributions deduced from the sequence of images for the ID 3 mm (a), 4 mm (b) and 6 mm (c) discharges for different input powers at 2 slm Ar gas flow rate conditions.

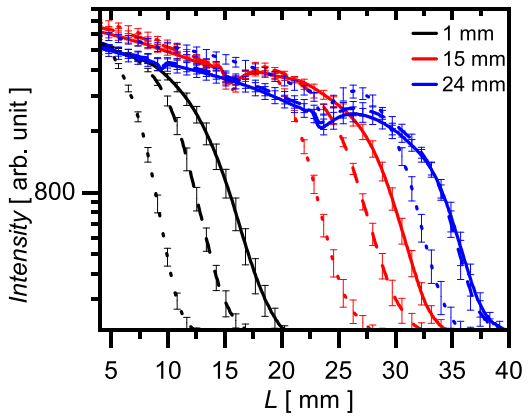


Figure 12. Axial emission intensity distributions for partially confined discharges sustained at 24 W in ID 4 mm tubes of different length when using 2 slm Ar and different cooling air flow rates: 0 slm (full lines), 10 slm (dashed lines) and 20 slm (dotted lines). The intensities are deduced from sequence of images recorded with the BF3 bandpass filter and 50 ms exposure time. The enhancement of the emission in the vicinity of the tube exit occurs due to the nitrogen emission not present inside the tube.

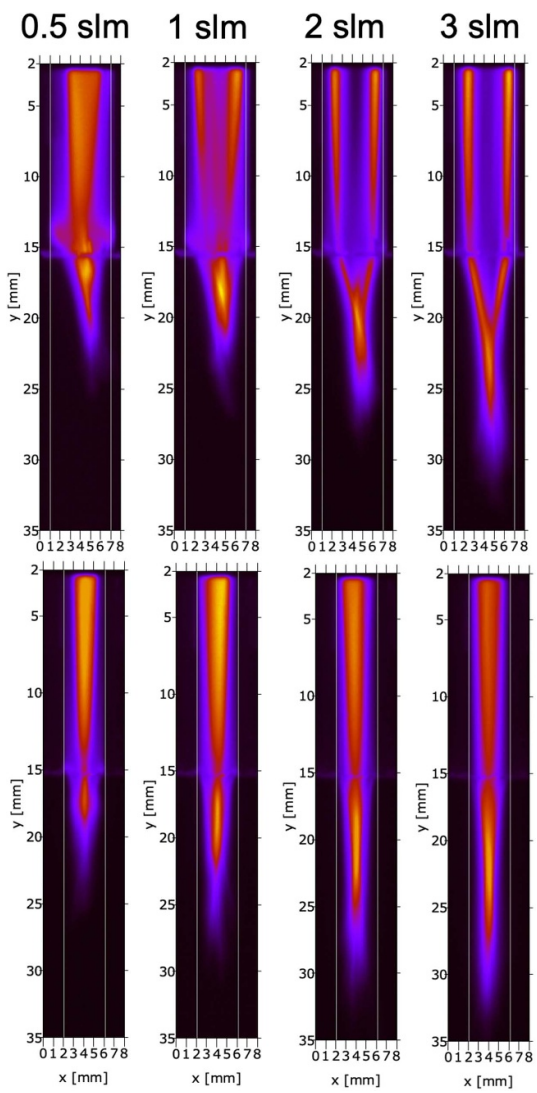


Figure 13. False-colour CCD images of discharges sustained with 24 W in tubes of 15 mm length and of ID 6 mm (1st row) and 4 mm (2nd row), respectively, using 10 slm cooling air and different Ar flow rates.

application possibilities of the partially confined discharge, the electron density along the plasma column has been determined, as described in section 2.2, in the case of a 14 mm long tube in comparison with the confined ($L = 44$ mm) discharge. As shown in figure 14(a), in the confined pure argon discharge the electron density slightly increases downstream the plasma column. The spatial profile of the electron density is similar to that of the gas temperature, shown in figure 14(b), since the dominant gas heating mechanism in argon discharges at atmospheric pressure is the elastic collisions, as also suggested by Kabouzi *et al* [46]. On the other hand, in the case of the partially confined discharge the electron density at the end of the discharge tube increases above the density of the confined discharge, and reaches a maximum in the middle of the plasma plume. The increase of the electron density occurs due to the inflow of molecular gases. With the increase of the collision frequency the power absorption also increases, which leads to the shortening of the plasma column compared to the confined plasma at the same input power. In the partially confined discharge the temperature distribution decouples from the electron density, since with the addition of the molecular gases vibrational-translational processes start playing a significant role in the gas heating.

The effect of oxygen is illustrated in the case of the confined discharge. With addition of 20 sccm O_2 into the 2000 sccm Ar flow (that is a Ar-1%O_2 initial gas mixture)[6], the electron density becomes about one order of magnitude higher compared to the Ar discharge, and monotonically decreases along the

[6] The addition of oxygen suppresses the OH emission used for estimation of the gas temperature, thus measurements at higher O_2 addition become impossible.

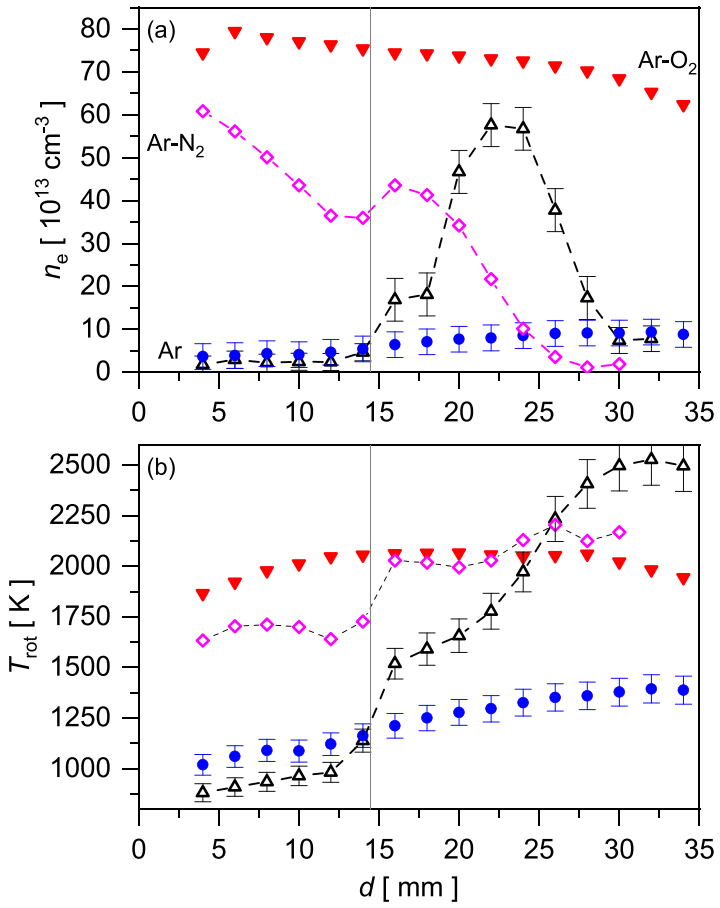


Figure 14. Axial distributions of the averaged electron density and rotational temperature for fully (full symbols) and partially (open symbol) confined discharges sustained with 25 W in 2 slm Ar, 2000 sccmAr–20 sccmO_2 and 2000 sccmAr–20 sccmN_2 gas mixtures, respectively. The vertical line marks the end of the discharge tube for the partially confined discharge. $d = 0$ denotes the position of the surfatron's end plate.

plasma column. In the case of N_2 addition (Ar-1%N_2), illustrated in the case of the partially confined discharge, the enhanced electron density decreases along the plasma column inside the tube, and exhibits an increase at the tube's exit and reaches a maximum closer to the tube than in the case of pure Ar discharge. At the same time, the plasma column is also shorter than in the case of Ar discharge. The temperature (determined from the rotation spectra of the 337 nm N_2 band) distribution is decoupled from that of the electron distribution, the enhanced temperature does not change significantly inside the tube, while increases in the plasma plume region. Similar trends have been observed for the electron density and temperature distributions in the case of a discharge sustained in a OD 4 mm, ID 1 mm and 8 mm long tube at 1 slm Ar with input powers in the range of 50–150 W by Garcia *et al* [35], and by Ridenti *et al* [25] for fully unconfined discharge ignited in OD 4 mm and ID 2 mm ceramic tube at 2.5 slm Ar with input powers in the range of 20–150 W.

As just presented, the average gas temperature in the discharge filament can reach high values. The heat transport around the discharge and in the afterglow can be visualised by Schlieren imaging, as described in section 2.1. We remind here, that in the vicinity of the surface-wave launching gap (see figure 1) the jet of cooling air hits the discharge tube, which afterward flows along the tube surface. In the case of the 20 slm air flow, in the vicinity of the surfatron the heat is very efficiently carried by the air flow downstream, since no significant rise in the ambient temperature is detected, i.e. no change in the refracted index of the air around the tube can be observed, as shown in figure 15(a). However, moving downwards, the gradual heating of the environment is observed. On the other hand, in the case of no air flow the convection of heat upwards to the surfatron body can be observed, as marked on figure 15(b). The images show that the expanding cone of the high temperature afterglow is well defined (figure 15(b)), which is surrounded by the heat transported by the air flow. In the case of the partially confined discharge the slant angle of the expanding cone is similar to that of the confined discharge, however the expansion is more diffuse, which may indicate a faster temperature decrease axially.

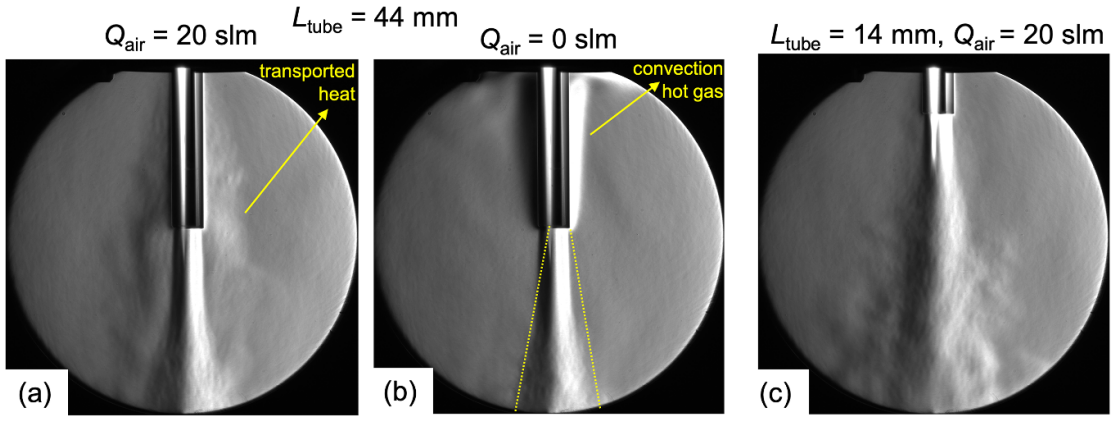


Figure 15. Schileren images of the confined and partially confined discharges under different cooling air conditions. Images are taken by using the BF2 bandpass filter.

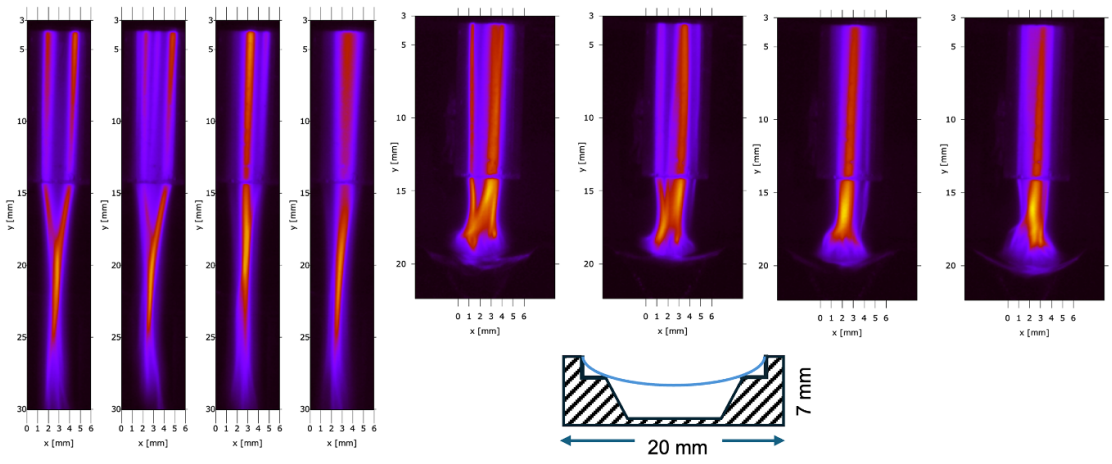


Figure 16. Sequence of false-colour CCD images of the freely propagating plasma column and the plasma plume in contact with water flowing in an open channel positioned at 4 mm distance. The length of the discharge tube is 14 mm, input power 24 W, Ar flow rate 2 slm. Images are taken with 10 ms exposure time with the BF1 bandpass filter.

3.3. Plasma in contact with liquid

As already mentioned, the plasma is brought in contact with liquid with the aim to deposit the gas phase reactive species created in the plasma into the liquid. It has previously been shown in [16, 41] that in the case of the SWDs the species deposition can be controlled through the distance between the discharge tube and the liquid surface, namely: with increasing the distance the deposition of H_2O_2 in the liquid is decreased, while that of nitrite and nitrate are increased. The main creation pathway of H_2O_2 has been associated to the electron dissociation of H_2O at the plasma–liquid interface, which is controlled by the electron density in the plasma column at the interaction point.

Figure 16 shows the images of the freely propagating plasma column and the plasma plume brought in contact with water flowing in an open channel. The distance between the discharge tube and channel is 4 mm, while the concave meniscus of the flowing water is at a 6 mm distance. The images are recorded with the BF1 bandpass filter (350–550 nm) in order to emphasise the emission of nitrogen in the plasma plume and reduce the overall argon emission intensity. The exposure time is 10 ms, which does not allow to resolve the dynamics of the filaments, however makes possible to visualise the surface area the filaments cover during the interaction.

The images indicate that while in the discharge tube the plasma column retains the operation properties, the contracted plasma plume expands when got in contact with the water. The plasma filaments cover an ≈6 mm diameter circular area on the liquid surface. The discharge sustaining surface-wave, which propagates along the boundary of plasma column and the surrounding dielectric stops at the water surface, thus hinder the further development of the plasma column. According to the calculations of Benova *et al* [47], in order the plasma to penetrate the water surface, powers in the range of 1 kW are needed due to the very high dielectric permittivity of water $\epsilon = 80$. However, it is not clear if in the

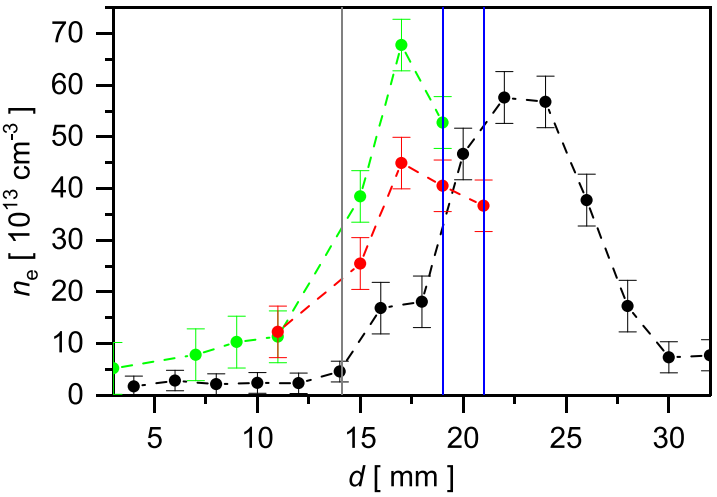


Figure 17. The axial electron density distribution for the freely propagating plasma column (black symbol) and in contact with water, respectively, at 25 W, 2 slm Ar and 20 slm cooling air conditions. The gray line marks the end of the discharge tube, the blue lines mark the different positions of the water surface.

mentioned case the plasma is sustained in water vapour or in the gas stream injected into the liquid. Nevertheless, at conditions resulting in high gas velocities (e.g. ID $\leqslant$ 3 mm and $Q \geqslant$ 2 slm) a cavity can form in the water surface, where the surface-wave and consequently, the plasma column can propagate further, similarly as in the case of the plasma jets [16, 48].

When bringing the plasma plume in contact with the liquid, as shown in figure 16, the same input power is applied as in the case of the freely propagating plasma column. As the wave propagation is suppressed by the liquid surface, the power absorption per unit length shall be higher along the shorter plasma column. The higher power absorption implies also higher electron density, as already discussed in previous Sections. Figure 17 shows the electron density in the plasma column in contact with the flowing liquid in comparison to that of the freely propagating plasma column. As expected, the electron density in the plasma plume in contact with the water surface enhances. By placing the water surface closer to the discharge tube, further enhancement of the electron density is achieved all along the plasma column. At the same time the rotational temperature of OH also increases. The enhancement of the OH rotational temperature has also been measured by Marinova *et al* [49] in the plasma plume when approached to the water surface.

In open channels, as one shown in figure 16, relatively stable flowing conditions can be achieved even with the use of peristaltic pumps, as long as the system is carefully designed. However, in the case of a closed channel—that is a pipe like channel with a surface opening at the interaction point—the pulsation of the liquid surface occurs due to the pressure induced by the peristaltic pump and carried through the closed pipe. This pulsation has been used to trap the plasma afterglow between liquid columns—and thus to enhance the interaction time—in the case of the interaction of the COST plasma jet (parallel positioned) with a microfluidic channel [50]. The SWD in contact with the liquid follows the pulsation of its surface. In this way, during the treatment of the pulsating liquid surface, the plasma conditions change (as shown in figure 17), and the control of the species deposition (i.e. the control of the plasma-treated liquid's composition) is lost.

During the plasma–liquid interaction the evaporation of the water is expected. Under moderate flow conditions the water vapour can enter the plasma region and result in the creation of OH molecules through electron dissociation of H_2O. Figure 18 shows the spectra in the 300–390 nm range—i.e. OH($A^2\Sigma^+$—$X^2\Pi$) and N_2 2nd positive bands—recorded at different positions in the plasma plume in contact with flowing water, and for the freely propagating plasma, respectively. The enhancement of the OH emission—originally existing due to the water impurity present in the discharge system—is detected only within the 2 mm vicinity of the water surface. The spectra measured at 3 mm distance from the water surface does not differ significantly from the spectra of the freely propagating plasma plume measured at the same plume position.

The effect of the liquid surface on the plasma gas flow can be illustrated through Schlieren imaging. Schlieren images have been recorded during the interaction of the plasma plume with water surfaces exhibiting different meniscus, as shown in figure 19. The water is hold by a 10 mm$\times$10 mm cuvette.

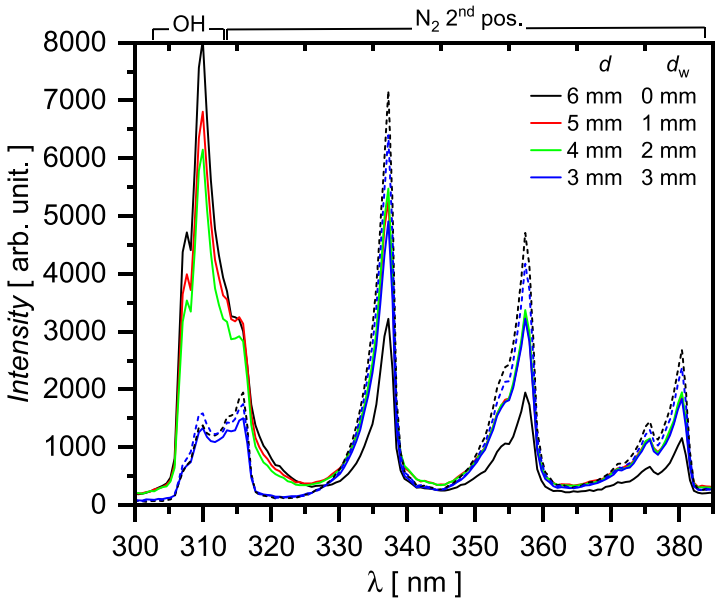


Figure 18. Low resolution spectra measured at different positions in the plasma plume in contact with water (full lines) and in the freely propagating plasma (dashed lines), respectively. d distance is measured from the end of the discharge tube and d_w denotes the distance from the water surface. The concave water meniscus is positioned at 6 mm distance from the discharge tube. The spatial resolution is 1 mm. The spectra are measured with Avantes spectrometer (AvaSpec-ULS2048x64TEC-EVO) with a 20 μm entrance slit.

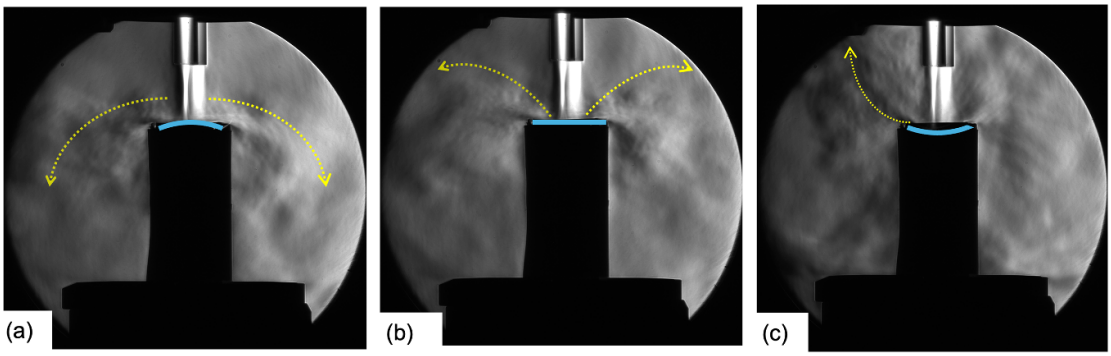


Figure 19. Schlieren images of the plasma plume in contact with water surfaces exhibiting different meniscus. The water is hold by a 10 mm × 10 mm cuvette.

Generally, the gas flow follows the interacting surface curvature. In the case of convex water meniscus, where the water surface lies above the edge of the cuvette, the gas following the water surface flows downwards at the edge of the cuvette (see figure 19(a)). In this case most of the water vapour is expected to leave the plasma region. When the meniscus is flat (figure 19(b)), the edge of the cuvette deflects the gas in a wide angle both upwards and downwards. On the other hand, the concave meniscus, when the size of the container is comparable to that of the plasma plume, can favour the mixing of the water vapour into the plasma plume, as indicated by the gas flow in figure 19(c). That is the case of the water flowing in the open channel presented above.

When using large containers the meniscus is approximately flat in a large area around the interaction zone, and the gas traveling along the surface is deflected by the edge of the container. The surface diffusion and the flow of afterglow along the surface favour the interfacial chemistry along the water surface. This is illustrated in the case of a 70 mm diameter beaker filled with pH indicator solution BDH '4.5'. The indicator solution has a deep blue colour at pH 6.0, bluish–gray at pH 4.6, orange–gray at pH 4.4 and orange-red at pH 3.5. According to figure 20 the acidification of the treated solution occurs on the whole water surface covered by the afterglow plasma. Near the walls the formation of a vortex can be observed, which can be related to the deflection of the gas flow at the container's edge. Due to this

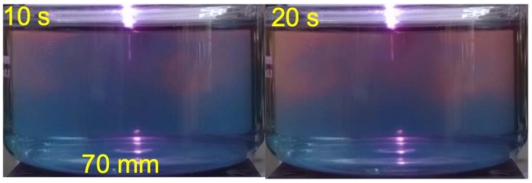


Figure 20. Sequence of images of the plasma plume's interaction with pH indicator solution used to visualise the kinetics of the species deposition into the liquid.

plasma induced vortex, the mixing of the liquid occurs during treatment, however it does not homogenise it. Without additional mixing an over-acidified layer is formed at the interface, which determines the chemical kinetics in the liquid phase during treatment. For example, the reaction rate of the $NO_2^- + H_2O_2 + H^+ \longrightarrow NO_3^- + H_2O + H^+$ process can significantly increase in this region. This effect gives the main difference between the treatment of batch and flowing liquids. These findings also show the main advantage of the SWD system comparing to the DC discharges and plasma jets, where the acidification has been shown to appear only at the impingement point [51, 52].

4. Conclusions

The operation mode of the low-power SDW has been studied for different diameter tubes under a wide range of input power and gas flow conditions, in order to determine conditions where a single filament discharge operation can be achieved, while also maximizing the width of the filament. Meanwhile, the macroscopic behaviour and the dynamics of the discharges have been illustrated. The transition from the fully confined to the partially confined discharge has been followed, and the effect of the transition on the axial electron density distribution has been determined. Related to the application of the SWDs for liquid treatments, the effect of the liquid surface on the plasma propagation and properties, and on the afterglow gas flow has been clarified.

Operation mode

- With increasing the tube diameter, from 3 mm to 6 mm, the power range where a single filament operation can be achieved shrinks, while the appearance of the second filament leads to the shortening of the plasma column. On the other hand, the single filament plasma column and plasma plume, respectively, become more contracted when tube diameter is decreased to 3 mm.
- The filamentation, i.e. splitting of the main filament, occurs with increasing the input power and the gas flow rate. The threshold for both the input power and gas flow rate are tube diameter dependent.
- For application purposes gas flow rates higher than 1 slm are required, since at lower gas flow rates the plasma column is more contracted and the plasma plume of the partially confined discharge is very short, which limits its application. Furthermore, the properties of the plasma plume are determined by the air inflow, which can be controlled through the flow rates of the main gas used and of the shielding air, respectively.

Although a full optimisation work has not been carried out, it is concluded that the ID 4 mm tube offers the wider range for tuning the plasma–liquid interaction.

Plasma characteristics

- The axial distribution of the electron density in the fully confined discharge is correlated with the temperature distribution, as the main heating mechanism can be associated to the inelastic electron collisions.
- In the partially confined discharge outside the discharge tube in the plasma plume the electron density decorrelates from the temperature distribution as a result of the new heating mechanism of the vibrational-translational collisions of air molecules.
- In the plasma plume the enhancement of the electron density occurs and exhibits a maximum in the middle of the plume. The enhanced power absorption due to the increased electron density is compensated by the shortening of the plasma column.

Plasma–liquid interaction

- The electron density in the plasma plume is further enhanced when the partially confined discharge is brought in contact with the liquid surface. The propagation of the surface-wave stops at the water

surface, which leads to the shortening of the plasma column and increase of power absorption per unit length all along the plasma column.
- The contraction of the plasma plume ceases when brought in contact with liquid surface, and the filaments cover a surface area comparable to that of the discharge tube.
- The afterglow flow follows the liquid meniscus and it is deflected accordingly at the edge of the container, while influences the vapour admixture into the plasma and enhances the interfacial processes along the liquid surface.

It can be concluded, that the electron density can be controlled at the interaction surface with the distance between the discharge tube and the liquid surface, while the deposition of the neutral species can be enhanced with the increase of the liquid surface covered by the afterglow flow.

Data availability statement

All data that support the findings of this study are included within the article (and any supplementary files).

Acknowledgments

The work has been supported by the Hungarian Science Foundation NKFIH, through Project K-132158.

ORCID iDs

Kinga Kutasi 0000-0001-6082-1853
Cédric Nöel 0000-0001-8651-1423
Thierry Belmonte 0000-0002-8572-7676
Péter Hartmann 0000-0003-3572-1310

References

[1] Bruggeman P J *et al* 2016 Plasma-liquid interactions: a review and roadmap *Plasma Sources Sci. Technol.* **25** 053002
[2] Vesna V, Kovačević V V, Sretenović G B, Obradović B M and Kuraica M M 2022 Low-temperature plasmas in contact with liquids: a review of recent progress and challenges *J. Phys. D: Appl. Phys.* **55** 473002
[3] Traylor M J, Pavlovich M J, Karim S, Hait P, Sakiyama Y, Clark D S and Graves D B 2011 Long-term antibacterial efficacy of air plasma- activated water *J. Phys. D: Appl. Phys.* **44** 472001
[4] Kang M H, Jeon S S, Shin S M, Veerana M, Ji S-H, Uhm H-S, Choi E-H, Shin J H and Park G 2019 Dynamics of nitric oxide level in liquids treated with microwave plasma-generated gas and their effects on spinach development *Sci. Rep.* **9** 1011
[5] Gierczik K, Vukusic T, Kovács L, Székely A, Szalai G, Milosevic S, Kocsy G, Kutasi K and Galiba G 2020 Plasma-activated water to improve the stress tolerance of barley *Plasma Process. Polym.* **17** 1900123
[6] Sardella E, Veronico V, Gristina R, Grossi L, Cosmai S, Striccoli M, Buttiglione M, Fracassi F and Favia P 2021 Plasma treated water solutions in cancer treatments: the contrasting role of RNS *Antioxidants* **10** 605
[7] Laurita R, Contaldo N, Zambon Y, Bisag A, Canel A, Gherardi M, Laghi G, Bertaccini A and Colombo V 2021 The use of plasma-activated water in viticulture: induction of resistance and agronomic performance in greenhouse and open field *Plasma Process. Polym.* **18** 2000206
[8] Bilea F, Bradu C, Cicirma M, Medvedovici A M and Magureanu M 2024 Plasma treatment of sulfamethoxazole contaminated water: intermediate products, toxicity assessment and potential agricultural reuse *Sci. Total Environ.* **909** 168524
[9] Magureanu M, Bilea F, Bradu C and Hong D 2021 A review on non-thermal plasma treatment of water contaminated with antibiotics *J. Hazardous Mater.* **417** 125481
[10] Marotta E and Paradisi C 2025 The importance of mechanistic studies in the development of cold plasma-based degradation of persistent organic pollutants in water *Curr. Opin. Green Sustain. Chem.* **52** 100999
[11] Omran A V, Busco G, Ridou L, Dozias S, Grillon C , Pouvesle J-M and Robert E 2020 *Plasma Sources Sci. Technol.* **29** 105002
[12] Skoro N, Kutasi K, Puac M and Petrovic Z L Puac N 2024 Effect of target material on electrical properties of a two-electrode dielectric barrier helium plasma jet *Plasma Sources Sci. Technol.* **33** 045015
[13] Slikboer E and Walsh J 2021 Impact of electrical grounding conditions on plasma-liquid interactions using Thomson scattering on a pulsed argon jet *Sci. Rep.* **11** 17749
[14] Ryan C T, Darhuber A A, Kunnen R P J, Gelderblom H and Sobota A 2024 Electrical properties determine the liquid flow direction in plasma-liquid interactions *Sci. Rep.* **14** 17152
[15] Morabit Y, Hasan M I, Whalley R D, Robert E, Modic M and Walsh J L 2021 A review of the gas and liquid phase interactions in low-temperature plasma jets used for biomedical applications *Eur. Phys. J. D* **75** 32
[16] Kutasi K, Popović D, Krstulović N and Milošević S 2019 Tuning the composition of plasma-activated water by a surface-wave microwave discharge and a kHz plasma jet *Plasma Sources Sci. Technol.* **28** 095010
[17] Moisan M and Zakrzewski Z 1991 Plasma sources based on the propagation of electromagnetic surface waves *J. Phys. D: Appl. Phys.* **24** 1025
[18] Granier A, Pasquiers S, Boisse-Laporte C, Darchicourt R, Leprince P and Marec J 1989 Characterisation of a low-pressure oxygen discharge created by surface waves *J. Phys. D: Appl. Phys.* **22** 1487
[19] Guerra V and Loureiro J 1999 Kinetic model of a low-pressure microwave discharge in O2-H2 including the effects of O- ions on the characteristics for plasma maintenance *Plasma Sources Sci. Technol.* **8** 110

[20] Kutasi K, Noel C, Belmonte T and Guerra V 2016 Tuning the afterglow plasma composition in Ar/N2/O2 mixtures: characteristics of a flowing surface-wave microwave discharge system *Plasma Sources Sci. Technol.* **25** 055014
[21] Ricard A, Besner A, Hubert J and Moisan M 1988 High nitrogen atom yield downstream of an atmospheric pressure flowing Ar-N, microwave discharge *J. Phys. B: At. Mol. Opt. Phys.* **21** L579–83
[22] Moisan M, Paxtel R and Huber J 1990 Propagation of a surface wave sustaining a plasma column at atmospheric pressure *Contrib. Plasma Phys.* **30** 293–314
[23] Galante L J, Selby M and Hieftj G M 1988 A low-power surfatron source for the atomic-emission- spectrometric detection of non-metals in aqueous solution *Appl. Spectrosc.* **42** 559
[24] Krčma F, Tsonev I, Smejkalová K, Truchlá D, Kozáková Z, Zhekova M, Marinova P, Bogdanov T and Benova E 2018 Microwave micro torch generated in argon based mixtures for biomedical applications *J. Phys. D: Appl. Phys.* **51** 414001
[25] Ridenti M A, Souza-Corre J A and Amorim J 2014 Experimental study of unconfined surface wave discharges at atmospheric pressure by optical emission spectroscopy *J. Phys. D: Appl. Phys.* **47** 045204
[26] Castaños-Martinez E, Kabouzi Y, Makasheva K and Moisan M 2004 Modeling of microwave-sustained plasmas at atmospheric pressure with application to discharge contraction *Phys. Rev. E* **70** 066405
[27] Kabouzi Y, Calzada M D, Moisan M, TranK C and Trassy C 2002 Radial contraction of microwave-sustained plasma columns at atmospheric pressure *J. Appl. Phys.* **91** 1008
[28] Lishev St Shivarova A and Tarnev K 2008 Spatial distribution of the wave field of the surface modes sustaining filamentary discharges *J. Appl. Phys.* **103** 013304
[29] Hnilica J, Kudrle V, Vašina P, Schäfer J and Aubrecht V 2012 Characterization of a periodic instability in filamentary surface wave discharge at atmospheric pressure in argon *J. Phys. D: Appl. Phys.* **45** 055201
[30] Moisan M, Beaudry C and Leprince P 1975 A small microwave plasma source for long column production without magnetic field *IEEE Trans. Plasma Sci.* **PS3** 55
[31] Gigosos M A and Cardeñoso V 1996 New plasma diagnosis tables of hydrogen Stark broadening including ion dynamics *J. Phys. B: At. Mol. Opt. Phys.* **29** 4795
[32] Descoeudres A 2006 *PhD EPFL* 10.5075/epfl-thesis-3542
[33] Yubero C, Garcia M C and Calzada M D 2006 On the use of the H spectral line to determine the electron density in a microwave (2.45 GHz) plasma torch at atmospheric pressure *Spectrochim. Acta B* **61** 540–4
[34] Ricard A, St-Onge L, Malvos H, Gicquel A, Hubert J and Moisan M 1995 Torche a plasma a excitation micro-onde: deux configurations complementaires *J. Phys. III* **5** 1269
[35] Garcia M C, Yubero C, Calzada M D and Martinez-Jimenez M P 2005 Spectroscopic characterization of two different microwave (2.45 GHz) induced argon plasmas at atmospheric pressure *Appl. Spectrosc.* **59** 519
[36] Happold J, Lindner P and Roth B 2006 Spatially resolved temperature measurements in an atmospheric plasma torch using the A-X OH *J. Phys. D: Appl. Phys.* **39** 3615
[37] Bruggeman P J, Sadeghi N, Schram D C and Linss V 2014 Gas temperature determination from rotational lines in non-equilibrium plasmas: a review *Plasma Sources Sci. Technol.* **23** 023001
[38] Bloyet E, Eprince P, Llamas Blasco M and Marec J 1981 Ionization by pulsed plasma surface wave *Phys. Lett.* **83A** 391
[39] Selby M and Hiefts G M 1987 Taming the surfatron *Spectrochim. Acta B* **42** 285
[40] Margot-Chaker J , Moisan M, Chaker M, Glaude V M M, Lauque P, Paraszczak J and Sauve G 1989 Tube diameter and wave frequency limitations when using the electromagnetic surface wave in the m = 1 (dipolar) mode to sustain a plasma column *J. Appl. Phys.* **66** 4134
[41] Kutasi K, Bencs L, Tóth Z and Milošević S 2023 The role of metals in the deposition of long-lived reactive oxygen and nitrogen species into the plasma-activated liquids *Plasma Process. Polym.* **20** 2200143
[42] Kutasi K, Péter L and Thót Z 2024 Plasma-deposited reactive species assisted synthesis of colloidal zinc-oxide nanostructures *J. Phys. D: Appl. Phys.* **57** 315201
[43] Rumbach P and Go D B 2017 Perspectives on plasmas in contact with liquids for chemical processing and materials synthesis *Top. Catal.* **60** 799–811
[44] Elg D T, Delgado H E, Martin D C, Sankaran R M, Rumbach P, Bartels D M and Go D B 2021 Recent advances in understanding the role of solvated electrons at the plasma-liquid interface of solution-based gas discharges *Spectrochim. Acta B* **186** 106307
[45] Oldham T and Thimsen E 2022 Electrochemical structure of the plasma?liquid interface *J. Phys. Chem. C* **126** 1222–1229
[46] Kabouzi Y, Graves D B, Castanos-Martinez E and Moisan M 2007 Modeling of atmospheric-pressure plasma columns sustained by surface waves *Phys. Rev. E* **75** 016402
[47] Benova E, Atanasova M, Bogdanov T, Marinova P, Krčma F, Mazankova V and Dosta L 2016 Microwave plasma torch at a water surface *Plasma Med.* **6** 59–65
[48] Kawamoto H , Umezu S 2005 Electrohydrodynamic deformation of water surface in a metal pin to water plate corona discharge system *J. Phys. D: Appl. Phys.* **38** 887–94
[49] Marinova P, Benova E, Topalova Y, Todorova Y, Zhekova M, Yotinov I and Krcma F 2023 Effects of surface-wave-sustained argon plasma torch interaction with liquids *Processes* **11** 3313
[50] Bissonnette-Dulude J, Heirman P, Coulombe S, Bogaerts A, Gervais T and Reuter S 2024 Coupling the COST reference plasma jet to a microfluidic device: a computational study *Plasma Sources Sci. Technol.* **33** 015001
[51] Rumbach P, Griggs N, Sankaran R M and Go D B 2014 Visualization of electrolytic reactions at a plasma-liquid interface *IEEE Trans. Plasma Sci.* **42** 2610–1
[52] Brubaker T R, Ishikawa K, Kondo H, Tsutsumi T, Hashizume H, Tanaka H, Knecht S D, Bilén S G and Hori M 2019 Liquid dynamics in response to an impinging low-temperature plasma jet *J. Phys. D: Appl. Phys.* **52** 075203